Time-dependent volumetric printing of precision lenses through dynamic laser writing

OPEN ACCESS
IMMT | IOP Publishing
International Journal of Extreme Manufacturing
Int. J. Extrem. Manuf. **7** (2025) 045007 (15pp)
https://doi.org/10.1088/2631-7990/adbd0a

Time-dependent volumetric printing of precision lenses through dynamic laser writing

Chengxue Piao[1,§], Xiaotong Du[1,§], Ya Xu[1], Suet To[2], Limin Zhu[3] and Zhiwei Zhu[1,*]

[1] School of Mechanical Engineering, Nanjing University of Science and Technology, Nanjing 210094, People's Republic of China
[2] State Key Laboratory in Ultra-Precision Machining Technology, Department of Industrial and Systems Engineering, The Hong Kong Polytechnic University, Kowloon, Hong Kong SAR, People's Republic of China
[3] State Key Laboratory of Mechanical System and Vibration, School of Mechanical Engineering, Shanghai Jiao Tong University, Shanghai 200240, People's Republic of China

E-mail: zw.zhu@njust.edu.cn

Received 29 August 2024, revised 16 December 2024
Accepted for publication 4 March 2025
Published 2 April 2025

Abstract

The position-dependent feature in current vat photopolymerization-based additive manufacturing leads to challenges in controlling the dimensional accuracy of printed components. To overcome this intrinsic limitation, we propose a time-dependent dynamic laser writing (DLW) approach for the precise volumetric printing of complex-shaped lenses. In the DLW-based volumetric printing, the formed surface is generated by accumulating the material growth functions (MGFs) on the scanning path, where the MGF is created by the laser direct irradiation with controlled energy doses. Benefiting from the stability of MGFs and the process homogenization, the DLW is less sensitive to process errors when compared to current vat photopolymerization-based additive manufacturing techniques. Furthermore, the continuous scanning leads to the naturally ultra-smooth feature of the printed surfaces. As a demonstration, a millimeter-scale spherical lens was printed in 5.67 min, achieving a three-dimensional (3D) form error of 0.135 μm (root mean square, RMS) and a surface roughness of 0.31 nm (RMS). The printing demonstrated comparable efficiency while achieving form errors an order of magnitude smaller than those of state-of-the-art continuous layer-wise and volumetric printing methods. In addition, polymer lens arrays, freeform polymer lenses, and fused silica lenses were successfully printed, demonstrating promise for advancing the state-of-the-art in 3D printing of precision lenses.

§ These authors contributed equally to this work and should be considered co-first-author.
* Author to whom any correspondence should be addressed.

Supplementary material for this article is available online

Keywords: precision optics, additive manufacturing, volumetric printing, material growth function

1. Introduction

Precision optics are essential for a wide variety of systems that utilize light for both imaging and nonimaging applications[1]. In contrast to conventional material removal-based machining and plastic deformation-based forming techniques, additive manufacturing, also known as three-dimensional (3D) printing, has emerged as a promising tool for the rapid prototyping of customized complex-shaped refractive optics[2,3]. The processable optical materials for fast prototyping include polymers[4,5], silica glasses[6,7], and transparent ceramics[8,9] to mention a few.

Currently, vat photopolymerization is the mainstream technique for the additive manufacturing of precision optics[10],which can be categorized into pointwise, layerwise, and volumetric printing techniques based on material addition approaches. However, the resultant form accuracy, manufacturing eficiency, and surface smoothness are crucial for the practical application of the printed optics. The pointwise two-photon polymerization lithography (TPL), as a typical direct laser writing technique, is demonstrated to be powerful for the additive generation of complex-shaped optics with sub-micron form accuracy and sub-wavelength structure resolution[11,12]. However, the inherent point-by-point scanning feature of TPL leads to extremely low manufacturing eficiency. Additionally, the need for ultra-precision laser spot positioning systems substantially raises the costs of printing systems, posing challenges for practical industrial applications[13]. To overcome the efficiency limitation in the pointwise TPL, the layerwise printing in the projection stereolithography was developed, which is capable of improving the eficiency by several orders of magnitude. By adopting digitalmicromirror devices[14,15] or low-cost liquid crystal displays[4,16] for generating dynamic masks, the desired shapes can be concurrently solidified in each layer without the need for mechanical scanning. Although the layerwise printing can significantly speed up the shape formation, the over-long dwell time between the adjacent layers for resin separation and refilling can increase the overall processing time for manufacturing[4,17].

To avoid the time consumed between layers in projection stereolithography, continuous printing capable of printing components during continuous lifting was developed by regulating the interface adhesion properties[10,18,19]. However, the intermittent change of the dynamic masks during the lifting may inevitably generate pixelated and stair-stepping textures, which may deteriorate the printed surface quality. To suppress the undesired surface defects, a thin liquid film conformal to the printed shapes was purposely employed for coating the printed surfaces, which can lead to sub-nanometric surface roughness[10,20,21]. Since the meniscus equilibrium of the thin films is jointly determined by a complex set of factors, including the surface curvatures, resin viscosity, and sizes of surface defects[16,20], it is challenging to precisely predict the shapes of the printed parts with the adhered films. Moreover, the form accuracy for the continuously printed parts is sensitive to the interface property, as well as the accuracy of generated dynamic masks and lifting motions. These complex factors impose great difficulties in precisely controlling the printed shapes, yielding achievable form errors from a few micrometers to tens of micrometers.

By tomographically illuminating rotary photocurable resins from multiple angles in volumetric additive manufacturing, dynamically patterned light fields were superimposed within the volume to cure the desired shapes simultaneously, achieving a much shorter printing time at the scale of 10 s to 1 min for creating components sizing tens of millimeters[22–24]. However, owing to the chemical diffusion, light scattering, and optical blurring in the resin, the complex light attenuation and absorption inside the resin made it challenging to precisely control the structure dimensions and surface micro topographies for the tomographical additive manufacturing. Therefore, a complex light intensity compensation strategy was essentially required, which is highly dependent on the precise modeling of the nonlinear light-resin interactions[25–27]. An alternative volumetric printing method is to polymerize desired patterns by intersecting two laser beams with two different wavelengths. In the process, the resin is activated by a first wavelength while initiated or inhibited by the second wavelength, thereby being capable of generating volumetric structures through continuously varying the laser irradiation positions and patterns within the resin[28–30]. In this printing system, digital projectors[28] or laser scanning[29] using one wavelength generate the dynamic patterns within the light sheet with another wavelength. Although it is regarded as a linear volumetric additive manufacturing, the varying light patterns endow the process with layerwise features. Therefore, besides the requirement for the complex compensation for light intensities, the stair-stepping textures might be inevitably formed on the printed surfaces. In addition, although complex 3D structures were successfully generated by the tomographic and dual-wavelength printing, the achievable dimensional accuracy of the printed components was restricted to the level of tens of micrometers, which may significantly limit their applications in fields requiring high accuracy[23,31].

The challenging aspect of guaranteeing high form accuracy in 3D printing is essentially caused by the position-dependent

nature of current pointwise, layerwise, and volumetric techniques, where the printed shape is determined by the exact positions of photocuration. To overcome this fundamental limitation, we propose a time-dependent volumetric printing process using dynamic laser writing (DLW). In DLW, the laser irradiation time at specific positions is actively controlled to create a material growth function (MGF) with desired dimensions. By superimposing MGFs of varying sizes along the laser scanning path, curved surfaces with precisely controlled shapes can be achieved. Therefore, the component formation depends not only on the position but also on the dwell time of the laser spots. The distinctive features of the proposed DLW-based printing, which surpass existing pointwise, layerwise, and volumetric methods, can be summarized as follows.

(i) The distinguished time-dependent feature endows the printing process with less sensitivity to process operations, owing to factors including the stable dwell time-controlled MGFs that are insensitive to positioning errors and the process homogenization effect induced by accumulating all the MGFs with sizes much larger than the errors[32,33].
(ii) The continuous scanning with intervals significantly smaller than the spot size can produce smooth surfaces without the need for post-processing, inherently mitigating the undesired stair-stepping effects caused by the intermittent changes in conventional layerwise and volumetric printing.
(iii) The intricate phenomena of light attenuation and absorption within the resin are inherently accounted for in the MGFs. This allows for effective compensation by simply adjusting the laser irradiation times, thereby eliminating the need for complex light intensity compensation strategies that rely on precise modeling of nonlinear light-resin interactions in conventional volumetric printing.

In the remainder, we present the fundamental principles of DLW-based volumetric printing, including the characteristics of MGFs, the surface formation mechanism, and numerical simulations in Section 2. Section 3 showcases the printing of typical polymer and fused silica lenses. After the main conclusions drawn in Section 4, Section 5 provides detailed experimental setups and procedures.

2. Principle for DLW-based volumetric printing

The concept of MGF is crucial for the DLW-based volumetric printing, which is defined as the relationship between the geometry of the photocured footprint and the energy dose for the laser irradiation. In the DLW, a laser beam is scanned over the resin with a controlled irradiation energy dose (the product of the laser power and the irradiation time) to generate the MGFs, which are then accumulated in the spatial domain to construct the complex-shaped lenses.

2.1. Characteristics of the material growth function

The schematic of the developed DLW-based volumetric printing system is illustrated in Figure 1(a). The system employs a 405 nm UV laser as the energy source for solidifying the photocurable resins. During operation, the laser beam is oriented perpendicular to the resin surface. The resin pool is horizontally carried by two motorized precision stages configured in an orthogonal (X-Y) manner. The positions of the stages and the energy doses for the UV laser are controlled using pulse width modulation (PWM) methods. To coordinate the planar positions of the laser spot and the corresponding irradiation energy dose, a real-time control system is established to concurrently send PWM commands to the laser and motor drivers. Additionally, a glass slide is used to cover the resin container, which serves to hold the printed components and avoid surface fluctuations during the scanning process

Assume that the UV laser beam is nearly parallel, with a sufficiently small divergence angle that makes spot size changes in the curing region negligible, and that the beam's energy follows a Gaussian distribution after the collimation[34]. Therefore, the irradiation of the resin, as shown in Figure 1(b), will generate a 3D Gaussian-shaped polymerized footprint beneath the laser spot. This footprint can be defined as the MGF for the resin. The curing depth h and FWHM of the footprint inside the resin are closely related to the energy dose absorbed by the resin. With a laser beam with density of P_o, the energy dose E_δ in a single pulse is determined by the duty cycle δ and periodicity T of the PWM commands, namely $E_\delta = P_o\tau = P_o(\delta T)$, where τ denotes the dwell time. Therefore, dimensions of the MGFs can be actively controlled by tuning the duty cycles δ while maintaining a fixed periodicity. In the experiment, a periodicity of $T = 0.02$ s was used, and the 2D images of the generated MGFs were captured by an optical microscope with duty cycles ranging from 1% to 40%, as shown in Figure 1(c). The extracted footprint profiles from the 2D images exhibited Gaussian-like features, and the increased feature sizes corresponding to the increased duty cycles demonstrate the time-dependent nature of the photocuring process during laser writing. The orthogonality of Gaussian functions suggests that the MGFs have strong capabilities for reconstructing complex 3D surfaces[35,36]. This feature provides a solid foundation for printing precision optics by spatially superimposing MGFs with varying dimensions, generated using different duty cycles.

Assume $o_g - x_g y_g z_g$ is defined as a remote Cartesian coordinate system for the MGF. The laser axis is parallel to the z_g axis, and o_g is consistent with the laser spot center. Therefore, the MGF can be mathematically described at an arbitrary position (x, y) by

$$S(x_g, y_g, \delta) = \sum_{i=1}^{n} A_i(\delta) \exp\left(\frac{-\left(x_g^2 + y_g^2\right)}{2\sigma_i^2(\delta)}\right) \tag{1}$$

where $n = 2$ was purposely selected to describe the relatively large width close to the glass slide, which might be caused by the interface-induced light scattering effect. In addition, A_i and

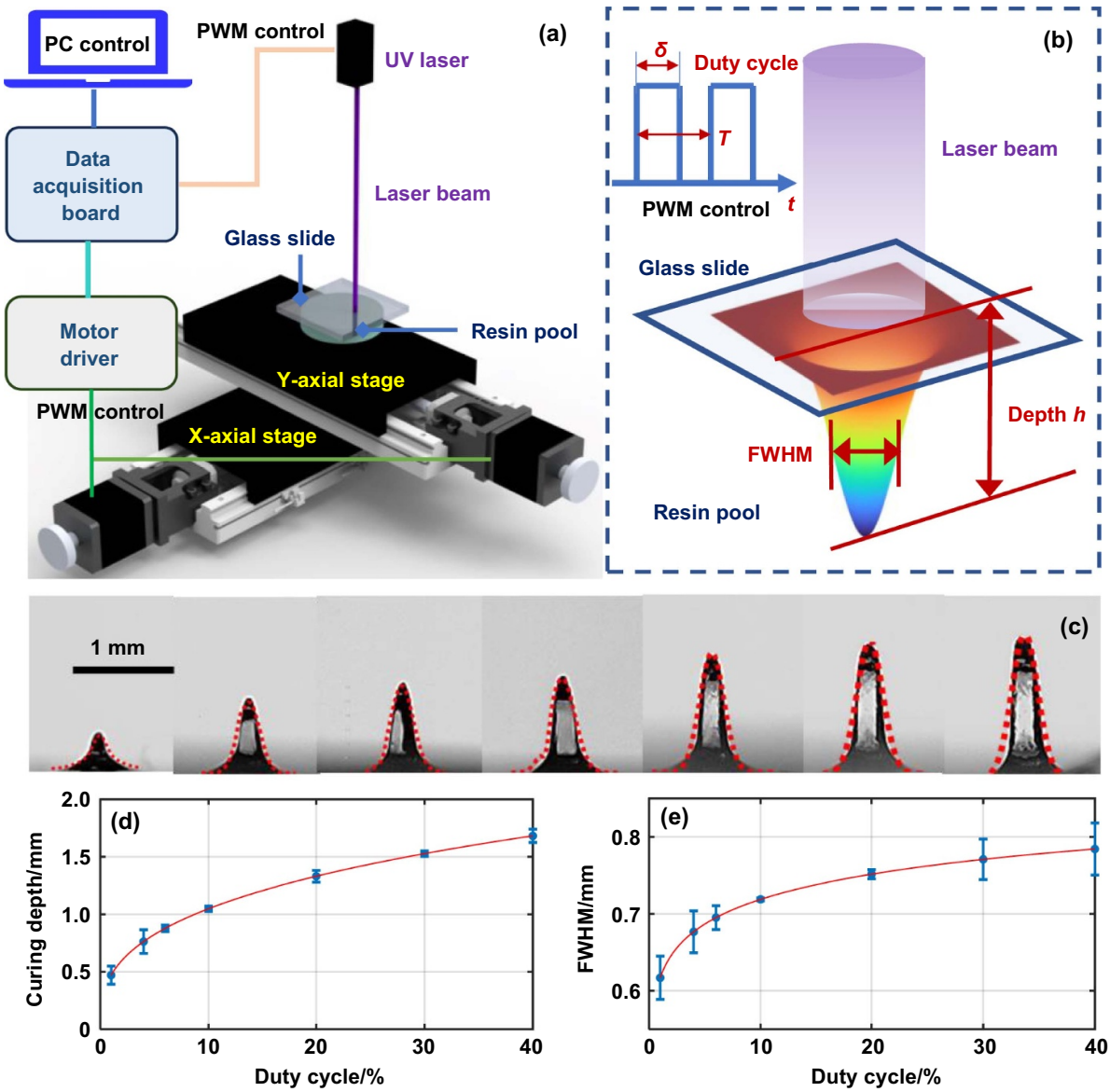

Figure 1. Features of the MGF in the DLW-based volumetric printing. (a) The system setup for the DLW. (b) Schematic of the MGF generation by a laser beam. (c) Photograph of the generated MGFs using various duty cycles. (d) The curing depth and (e) full width at half maximum (FWHM) of the MGFs nonlinearly related to the duty cycles, where the error bar denotes the standard deviation of the ten measured values for each duty cycle.

σ_i are the fitted coefficients for the footprint with a duty cycle of δ, which are obtained by the typical least-square fitting.

As shown in Figure 1(c), the best-fitted profiles of the printed MGFs align well with the Gaussian functions. The small discrepancy between the fitted and practical shapes can be attributed to several factors, including laser diffraction at the interfaces, imperfect energy distribution of the laser spot, nonlinear photo-curation, etc. To further investigate the relationship between the MGF dimensions and the duty cycles, ten repetitive single-spot curing experiments were conducted for each duty cycle. The statistical analysis of the curing depths and FWHMs of the MGFs is presented in Figures 1(d) and (e), respectively. With a stable laser and accurate PWM control, the relatively large error bars in Figures 1(d) and (e) may be caused by the non-ideal removal of residual resin on the MGFs when characterizing their feature sizes. Initially, the curing depths and FWHMs increase exponentially with the increase of the duty cycles. However, with further increase of the duty cycles, the feature sizes gradually approach saturation. This nonlinear increase and saturation phenomenon of the MGFs is caused by the complex energy dissipation during the continuous interactions between the photons and macro-molecules in the laser penetration, similar to other volumetric printing techniques[26]. Additionally, the results indicate that the printable depth may be limited to a few millimeters, and achieving greater depths may necessitate lasers with higher power to effectively penetrate the polymers.

2.2. Surface formation in DLW-based volumetric printing

The raster scanning path between the resin and laser is implemented in the DLW-based volumetric printing, and the laser beam retains vertical to the resin surface during the whole printing. The dwell points at the scanning grids are set to have lateral intervals of δ_x and δ_y, as shown in Figure 2(a). Taking any two dwell spots with a planar distance of $\delta_{x,y}$ (Figure 2(b)) for example, the laser at the spot p_1 that has a duty cycle of δ_1 may generate an MGF $S_1(x,y,\delta_1)$. When the laser spot moves to the second spot p_2 with a duty cycle of δ_2, the previously polymerized footprint exposed under the laser will not absorb energies, and the cross-linking for the resin will occur to superimpose on the previously solidified MGF $S_1(x,y,\delta_1)$, thereby forming a solidified component described by $S_p(x,y) = S_1(x,y,\delta_1) + S_2(x,y,\delta_2)$ in the global coordinate system $o-xyz$ for the resin, as schematically illustrated in Figure 2(b).

Similarly, when the laser scans along a linear direction, the generated MGFs along this direction will be superimposed to form a 2D component, as illustrated in Figure 2(c). Furthermore, this linear scan can be extended to the planar 2D raster scan, as presented in Figure 2(d). By varying duty cycles at dwell points, the corresponding MGFs grown from the X-Y plane that have controlled depths and FWHMs will be superimposed to construct a printed component with desired surface shapes in a volumetric manner. Meanwhile, the surface shapes can be precisely tuned by controlling the duty cycles $\delta(\eta,\varepsilon)$ at any dwell points (η,ε). Mathematically, the generated surface can be regarded as the convolution of the material growth rate and the equivalent irradiation time, which can be expressed in the global coordinate system $o-xyz$ by[32]

$$Z(x,y,\delta) = \iint_{\Omega} \frac{\partial S(x-\eta, y-\varepsilon)}{\partial \delta} \delta(\eta,\varepsilon)\,\mathrm{d}\eta\mathrm{d}\varepsilon. \tag{2}$$

To verify the volumetric printing, the linear scan was conducted using a harmonic command with gradually increased amplitude for the duty cycles, as illustrated in Figure 2(e). After the printing, the 2D image of the resultant structure was captured by a CCD camera and demonstrated in Figure 2(f). The practical profile was further extracted and shown in Figure 2(g), together with the theoretical one estimated by Equation (2). The spatial periodicity of the generated wavy structure was 1 mm, and the amplitude varied from 0.2 mm to 1.2 mm. From the profiles in Figure 2(g), a good accordance was achieved, and the slight deviation was jointly caused by the MGF uncertainties, positioning errors of the stages, and profile extraction errors, to mention a few. Nonetheless, the printed wavy structure well verified the effectiveness of the time-dependent DLW-based volumetric printing strategy.

Further, the 2D duty cycle distribution that is mathematically described by $\delta = \delta_0 \sin(2\pi f_0 x)\cos(2\pi f_0 y)$ was employed to print the 3D structure. The duty cycle exhibited a double harmonic grid shape as shown in Figure 2(h). In the printing, the lateral intervals for the dwell points were set as $\delta_x = \delta_y =$ 20 μm, and the amplitude and spatial frequency for the duty cycle δ were set as $\delta_0 = 0.38\ \mathrm{mm}^{-1}$ and $2\ \mathrm{mm}^{-1}$, respectively. Theoretically, the resultant spatial periodicity and amplitude for the generated structure were about 0.5 mm and 0.5 mm, respectively. Although it is challenging to capture the exact 3D micro-topography of the generated surface by the optical surface profiler, the printed surface in Figure 2(i) exhibited a similar grid feature as compared to the duty cycle in Figure 2(h). The result suggested that the DLW-based volumetric printing was capable of generating components with controllable 3D shapes by flexibly tuning the duty cycles, demonstrating a solid basis for printing bulk complex-shaped optics.

2.3. Printing lenses with specified surface shapes

2.3.1. Principle for generating specified surfaces. For printing a lens with a surface shape described by $\hat{Z}(x,y)$, the most essential thing is to inversely derive the duty cycle distribution. Mathematically, the inverse calculation can be treated as a minimization problem[32]:

$$\hat{\delta}(x,y) = \arg\min \| Z(x,y,\delta) - \hat{Z}(x,y) \| \tag{3}$$

where $\hat{\delta}(\mathrm{x},\mathrm{y}) \geqslant 0$, suggesting that there is no material removal in the laser irradiation.

Although there are a variety of algorithms for dealing with linear time-dependent processes[37,38], the highly nonlinear relationship between the MGFs and duty cycles, as illustrated in Figures 1(d) and (e), imposes great challenges in solving the minimization problem in Equation (3). Herein, inspired by the controlled volumetric removal as developed in optical polishing[39,40], the concept of equivalently controlling curing volume was proposed for the printing to inversely derive the duty cycles. More details about the solving process are presented in Section 5.5.

2.3.2. Simulation results and discussion. Via numerical simulation, a spherical lens with an aperture of 2 mm and a height of 0.15 mm was generated to demonstrate the effectiveness of the nonlinear inverse calculation for the duty cycles. A square region of size 2.4 mm × 2.4 mm was selected for printing the spherical lens, and the intervals for the dwell points were set as $\delta_x = \delta_y =$ 20 μm. Note that a slightly larger region was purposely selected for the calculation to avoid the undesired boundary effect that was inherently caused by the Gaussian reconstruction. After the inverse calculation, the theoretical surface shape was reconstructed by substituting the derived duty cycles into Equation (2). Accordingly, the form error was directly derived by comparing the desired and reconstructed surfaces in the same coordinate system, which was then shown in Figure 3(b). The peak-to-valley (PV) and root mean square (RMS) form errors for the theoretically reconstructed surface were, respectively, found to be around 8.5 μm and 2.1 μm, jointly owing to the boundary effect and non-ideal nonlinear calculation.

Obviously, the theoretical accuracy obtained from solving the nonlinear equation is far from the acceptable form accuracy required for optical applications. To achieve ultra-high

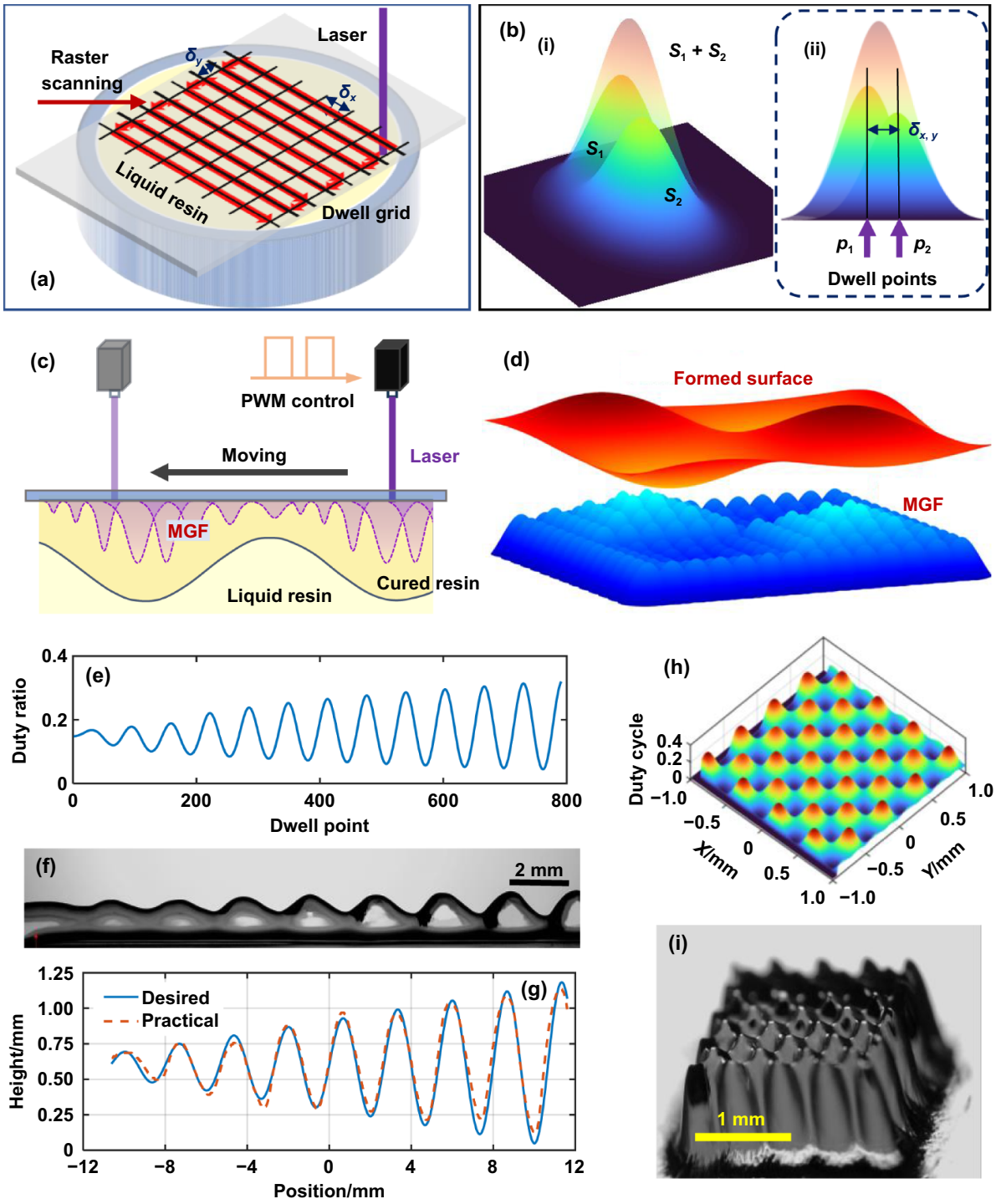

Figure 2. Principle illustration for the complex structure generation based on the DLW-based volumetric printing. (a) The relative raster scanning path for the printing. (b) The generated structure by adopting the laser at two dwell points p_1 and p_2 with different duty cycles: (i) its 3D configuration and (ii) the corresponding projected 2D superimposition. (c) Schematic of the 2D profile generation by superimposing the laser irradiation at 1D successive dwell points. (d) Schematic of the 3D form generation by adopting 2D dwell point distributions. (e) The duty cycle and (f) the 2D image of the corresponding harmonic profile with varying amplitudes. (g) A comparative illustration of the desired and practical 2D profiles using duty cycles in (e). (h) The 3D distribution of the duty cycles for printing. (i) The microscopic image of the correspondingly generated 3D grid surface.

accuracy for the form reconstruction, an iterative correction strategy inspired by the grayscale map correction method[16] was developed herein for better deriving the duty cycles. In this strategy, the form error difference related to the duty cycle difference in any two successive iterations was employed as the evolution gradient to iteratively correct the duty cycles. More details about deriving the iterative correction are presented in Section 5.6. The form error evolutions (PV and RMS)

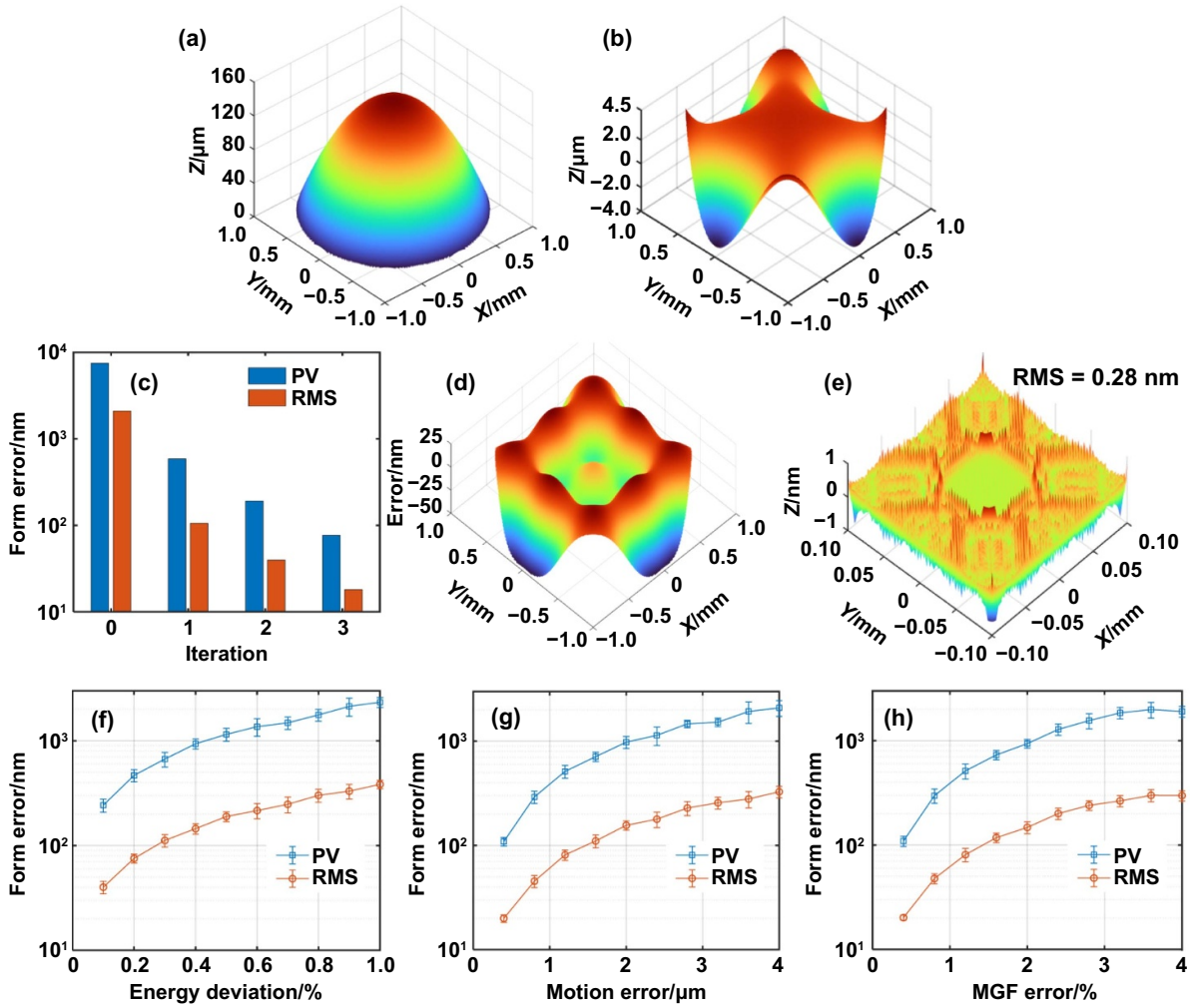

Figure 3. Numerical simulation results for printing a spherical optics by the DLW-based volumetric printing. (a) The desired spherical surface. (b) The form error using the calculated inverse duty cycle distribution. (c) The form error evolution during the iterative compensation. (d) The final error distribution after three iterations. (e) The theoretical surface roughness distribution. Form errors related to (f) the exposure deviations, (g) the positioning errors of the motorized stages, and (h) the instability of the MGFs.

for the reconstruction are illustrated in Figure 3(c). After the first iteration, the surface form error was dramatically reduced to be 587.3 nm (PV) and 105.65 nm (RMS). After three iterations, the reconstructed form errors were exponentially converged to be around 76.5 nm (PV) and 18.1 nm (RMS), resulting in the relatively uniform error distributions as demonstrated in Figure 3(d). In addition, after removing the best-fitted form from the reconstructed surface, a close-up view of the surface roughness topography is presented in Figure 3(e), showing a theoretically super-smooth surface with the roughness of 0.28 nm (RMS). Since the surface was mapped by continuously moving the laser spots, there will be intrinsically no stair-stepping or pixelated textures as commonly observed in conventional projection-based layerwise or volumetric printing.

For DLW-based volumetric printing, the form accuracy is jointly determined by the accuracy of energy doses (the PWM control for the duty cycles), the motion accuracy of the motorized stages, and the stability of the generated MGFs. To investigate the effect of these factors on the form errors, a Monte Carlo simulation was conducted by assuming that the deviations occurring at all the dwell points were in uniformly random distributions. For example, to mimic the laser energy dose errors within a specific value (0.1% for instance), a set of uniformly distributed random values (from −0.1% to 0.1%) were generated and added to the derived duty cycles for all the dwell points. By referring to Equation (2), the surface reconstruction simulations were repeated 30 times, using randomly generated parameter errors. The mean values of the resulting peak-to-valley (PV) and root mean square (RMS) form errors for all 30 simulations in each case were then recorded to characterize the sensitivity of the surface form errors to the system errors.

The simulation results in Figures 3(f)–(h) demonstrate the form errors associated with deviations in the duty cycles (energy doses), stage motions, and MGFs, respectively. The form errors were found to dramatically increase with the increase of these process errors. As shown in Figure 3(f), a

deviation of 0.4% (around tens of microseconds) for the duty cycles can lead to a form error of around 1 μm (PV). This level of duty cycle error can be well-controlled by current digital control systems. As illustrated in Figure 3(g), a motion error within ±2 μm, which is common for current precision stages, can lead to a form error of 1 μm (PV). This suggestes that components with relatively high form accuracy at the sub-microscale can be obtained by adopting even less precise scanning motions (at the microscale), potentially leading to a more cost-effective DLW system. Furthermore, a curing depth variation of 2% for the MGFs may lead to a form error of 1 μm (PV), suggesting that the printing process is less sensitive to the photocuration conditions, such as cross-linking temperature, homogeneity of the resins, and fluctuations of the laser energy. The results demonstrate that the time-dependent nature of the DLW provides it with less sensitivity to process errors, which can be attributed to both the position-insensitive MGFs and the process homogenization effect induced by accumulating all the MGFs with sizes much larger than the positioning errors[32,33].

Note: the laser spot size is crucial for printing, as it directly influences the dimensions of the generated GRFs. Typically, a much smaller spot size, in comparison to the surface feature sizes being printed, allows for finer surface reconstruction and accordingly better form accuracy. However, smaller spot sizes necessitate smaller grid sizes to achieve high surface smoothness, which can reduce printing efficiency. In contrast, larger spot sizes can accommodate larger grid sizes to create smooth surfaces. However, excessively large MGFs may result in surface over-fitting, significantly compromising printed form accuracy.

3. Results and discussion

3.1. Precision printing of typical lenses

3.1.1. Printing of spherical lenses. In practice, using a commercial photocurable resin, a spherical lens as simulated in Section 2.3 was fabricated by DLW. The scanning speed was set to 0.5 mm·s^{-1}, and the total printing time was approximately 5.67 min. A video recording the detailed printing process is presented in the Supplementary Information. The photograph of the printed lens, shown in Figure 4(a), exhibits a highly smooth surface with a clear image of the magnified background textures. By adopting a white light interference-based optical surface profiler with a 20× objective lens, the stitched 3D surface shape is presented in Figure 4(b). However, due to the accessible slope limitations of the profiler, only a 3D surface with a diameter of around 1 mm was captured. The cross-sectional profile of the printed lens is then compared with the designed profile in Figure 4(c), along with the profile deviation. The good agreement between the two profiles in Figure 4(c) suggests a high printing accuracy, with a maximum deviation of approximately 0.34 μm (PV). Furthermore, after removing the designed shape from the practically measured one, the 3D form error distribution is shown in Figure 4(d), resulting in PV and RMS errors of about 0.585 μm and 0.135 μm, respectively.

By employing a 50× objective lens, the 3D surface roughness component with a high lateral sampling resolution of 163 nm was extracted by removing the substrate shapes, as shown in Figure 4(e). The surface roughness was measured to be 0.31 nm (RMS), and the cross-sectional profile of the roughness component in Figure 4(f) was well within ±0.5 nm, demonstrating the super-smooth feature of the printed surfaces. After attaching the printed spherical lens to the objective lens of a smartphone, the magnified image of a leaf captured by the smartphone is shown in Figure 4(g). The clear view of the lattice textures on the leaf demonstrated the high performance of the printed lens for imaging applications. Furthermore, through the printed lens, a United States Air Force (USAF) 1951 resolution target was imaged by a CCD camera, and the enlarged erect image of the target is shown in Figure 4(h). A close-up view of the 6th and 7th groups of the elements is presented in Figure 4(i). The extracted intensity profile suggested that the 5th element in the 7th group could be well identified, which may correspond to a high imaging resolution of 203.2 lp·mm^{-1}. These results showcase the exceptional surface quality and imaging performance of the volumetrically printed lens, highlighting its potential for advanced optical applications.

For comparison, the performance of typical layerwise and volumetric printing methods is summarized in Table 1. Compared to the projection stereolithography method with meniscus equilibrium post-curing[4], our DLW-based printing achieves significantly shorter printing times—about an order of magnitude faster. Additionally, the form error is only about 10% of that obtained through stereolithography. In contrast, the printing time for DLW is comparable to continuous layerwise printing[10] and tomography volumetric printing[24], which eliminates the time between layers. The use of frustum layer stacking and blurred tomography strategies effectively improved surface roughness to less than 10 nm. However, the form errors in these methods were tens of times greater than those achieved with DLW. Overall, the comparison indicates that the proposed DLW-based printing offers excellent performance in terms of printing speed, form accuracy, and surface quality.

3.1.2. Printing of spherical lenses. To demonstrate the feasibility of printing lenses with complex shapes, a 5 × 5 lens array with a lenslet aperture of 1.2 mm and a pitch value of 1.5 mm was printed. The total printing time was approximately 24 min. The photograph of the printed lens array on a square substrate is presented in Figure 5(a). An imaging setup, as shown in Figure 5(b), was used to investigate the imaging performance of the printed lens array. As shown in Figure 5(c), although aberration-induced distortion with low resolutions was observed, a relatively uniform image array of the size-reduced alphabet "A" was achieved to showcase the strong printing capability. Furthermore, the focusing property of the lens array was examined by replacing the image target

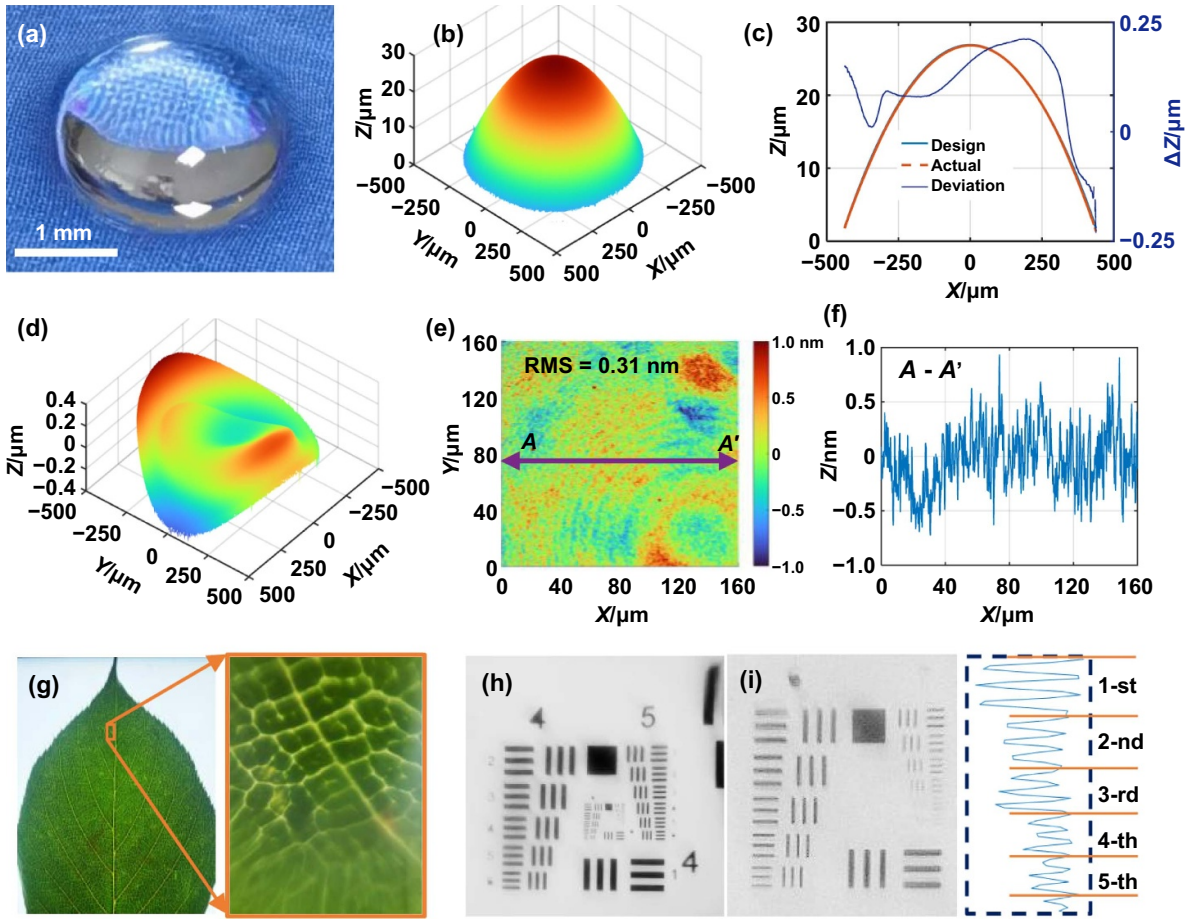

Figure 4. Results for printing a spherical lens by the DLW-based volumetric printing. (a) Photograph of the printed spherical lens. (b) The 3D shape of the lens captured by the optical surface profiler. (c) The cross-sectional profiles with the deviation related to the designed profile. (d) The 3D form error distribution. (e) The extracted 3D surface roughness component, (f) cross-sectional profile of the roughness component along the line A-A' as marked in (e). (g) Magnified view of leaf textures captured by attaching the printed spherical lens to a smart phone lens. (h) Image of a positive resolution target by a CCD camera. (i) A close-up view of the elements in Groups 6 and 7, together with the identified elements in Group7.

Table 1. Results obtained by different printing methods.

	Layerwise[4]	Continues[10]	Tomography[24]	DLW
Lenses	aspheric	spherical	spherical	spherical
Apertures	3 mm	1 mm	2.5 mm	2 mm
Printing time	hours	2 min	1 min	5.67 min
Form error (PV)	5.16 μm	14.7 μm	—	0.585 μm
Form error (RMS)	—	—	1.4 μm	0.135 μm
Roughness (RMS)	7 nm	3.4 nm	0.53 nm	0.31 nm

with a uniformly illuminated lamp, as schematically shown in Figure 5(d). The captured image of the focused spot is shown in Figure 5(e), and the corresponding normalized intensity distribution is presented in Figure 5(f). The sharp and uniform distribution of the light intensity demonstrated the high quality of the printed lens array. Although the lens array presented had a feature size in the millimeter scale, the DLW-based volumetric printing is capable of producing microlens arrays with much smaller feature sizes. This can be achieved by adopting laser sources with sufficiently small spot sizes.

In addition to the lens array, a freeform Alvarez lens was printed by the DLW technique, which was mathematically described by with $\hat{Z}(x,y) = A_1\left(\frac{1}{3}x^2 + xy^2\right) + A_2X + A_3$ with $A_1 = 0.05, A_2 = -0.5$, and $A_3 = 0.072$. The photograph of the printed freeform lens was shown in Figure 5(g). The image of linear grid lines captured through the printed lens, as shown in Figure 5(h-i), exhibited curved features that varied with the surface shapes. Through simulations using the commercial software Zemax, the simulated image in Figure 5(h-ii) showed good agreement with the practical image in figure 5(h-i). The

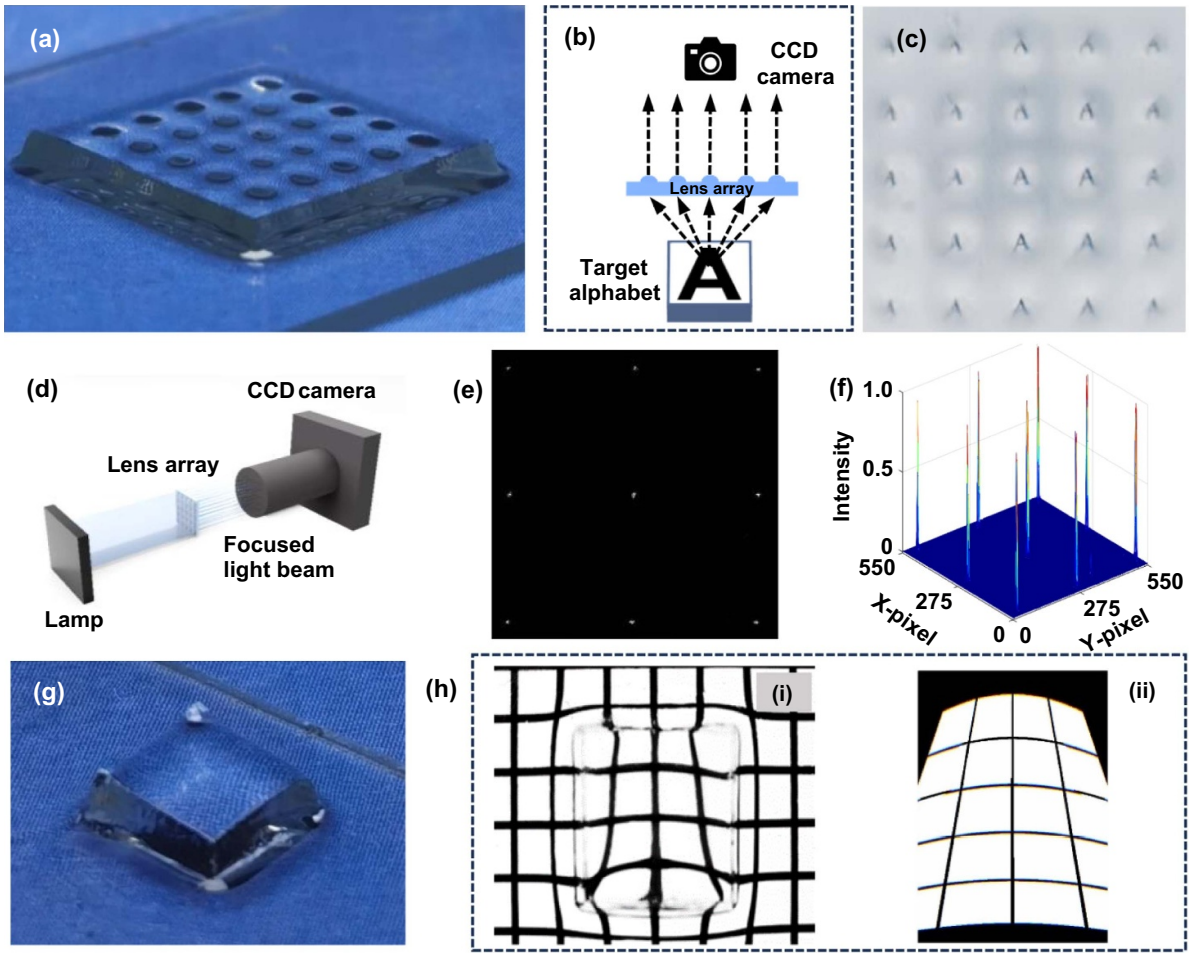

Figure 5. Results for printing complex-shaped lenses by the DLW-based volumetric printing. (a) Photograph of the printed lens array. (b) Schematic of the imaging system setup. (c) The captured image of the arrayed alphabet "A". (d) Schematic of the setup for characterizing the focus spots. (e) The captured focused spots. (f) The light density distribution of the focused spot through the lens array. (g) Photograph of the printed freeform Alvarez lens. (h) Comparison of (i) the measured and (ii) the simulated image of the linear grids through the freeform lens.

successful printing of the lens array and the freeform Alvarez lens well demonstrated the strong capability of the DLW-based volumetric printing technique to generate complex shaped lenses.

3.2. Printing of fused silica lenses

To demonstrate the feasibility for printing lenses with different materials, we tried to print fused silica lenses through processing the photocurable silica nanocomposite, which mainly consisted of the monomer matrix, the coupler for crosslinking, and the photoinitiator for structure curing[6,41,42]. The silica nanocomposite was demonstrated to be effective for printing complex shaped 3D components at the room temperature through the layerwise or volumetric stereolithography[6,23].

The flowchart for printing the fused silica lenses is illustrated in Figure 6(a). Before printing, the organic and inorganic materials were thoroughly stirred to create a homogeneous photocurable nanocomposite[6,41]. By treating the nanocomposite as a kind of printable material, the DLW-based printing was directly applied to generate the lenses (green parts) with desired surface shapes. The printed green part was then debinded by heating up to a temperature of 600 °C to fully vaporize the organic materials. The residual porous brown part after the debinding was further sintered to 1 260 °C in the air to get clear fused silica lenses with full densification. During the process, a nearly identical shrinkage of around 28% may occur along the horizontal and vertical directions. The detailed heating profiles for the debinding and sintering are illustrated in Figures 6(b) and (c), respectively. To achieve high form accuracy for the final fused silica components, the dimensions of the printed green parts were deliberately determined with shrinkage compensation.

After debinding, the printed silica spherical lens with high surface smoothness is photographically shown in Figure 7(a). The photographs of the side-view and top-view of the sintered clear fused silica lens are illustrated in Figure 7(b), exhibiting to be highly transparent with a clear image of the background. Similarly, the spherical lens with a smaller curvature after the debinding and sintering are, respectively, shown in Figures 7(c) and (d). Considering the measurement capability, the surface shape of the lens with a larger curvature in

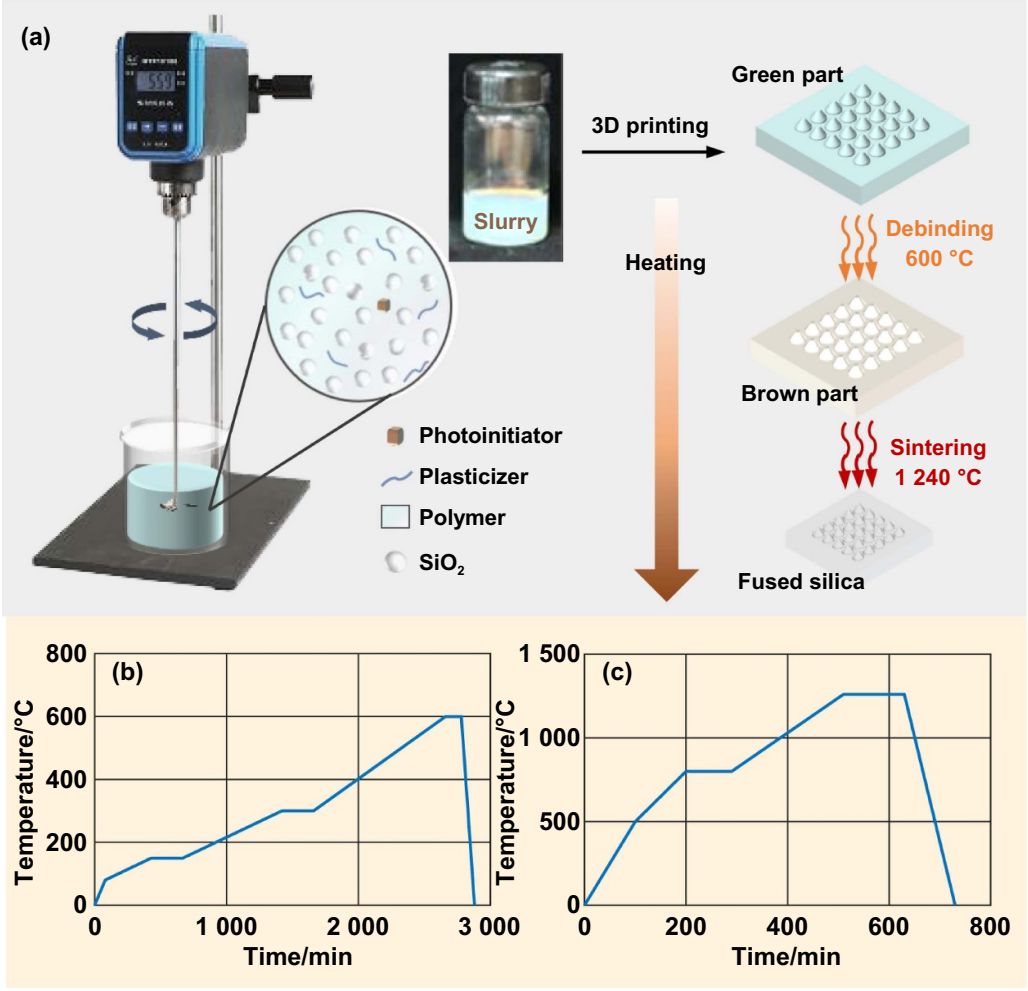

Figure 6. Process for printing the fused silica lenses. (a) Schematic of the printing process involving the nanocomposite preparation, 3D printing, and high temperature processing. The heating profiles for (b) the debinding and (c) sintering processes.

Figure 7(b) was characterized by the optical surface profiler with a 5× objective lens, resulting in the 3D surface form presented in Figure 7(e). As shown in Figure 7(e), there are null points that could not be reconstructed from the interference fringes owing to the over-large surface slopes of the printed lens. By removing the designed sphere, the resulting 3D form error distribution is illustrated in Figure 7(f), which is well within ±2.5 μm. Compared with the form error for the printed polymer lens in Figure 4(d), the relatively larger form error of the fused silica lens can be attributed to printing errors at room temperature, along with warpage and non-ideal shrinkage compensation during high-temperature processing.

Using a 50× objective lens, the detailed surface roughness of the printed fused silica lens was captured and presented in Figure 7(g). The surface exhibited no visible stair stepping artifacts from the printing process. The random surface textures were mainly formed during the high-temperature debinding and sintering processes. Statistically, the surface roughness was measured to be around 13.5 nm (RMS), which is suitable for optical applications. Compared to the printed polymer lenses, the relatively high roughness was primarily attributed to the inhomogeneous distribution of organic and inorganic materials, the sizes of the nano-powders, and airborne contaminants that adhered to the surfaces during high-temperature processing. To demonstrate the imaging capability, a clear building image was captured through the printed fused silica lens using a smartphone. As illustrated in Figure 7(h), the captured image shows a size-reduced and reversed feature, as expected for a spherical lens.

4. Conclusion

We report a time-dependent dynamic laser writing (DLW) approach for the volumetric 3D printing of precision optics. In the DLW process, a laser beam with controllable energy doses is scanned over a photosensitive resin, and the accumulation of the resulting position-varying material growth functions (MGFs) on the scanning path can directly form complex-shaped lenses in a volumetric manner.

To enable precise printing of lenses with specified forms, the nonlinear relationship between the MGFs and the laser

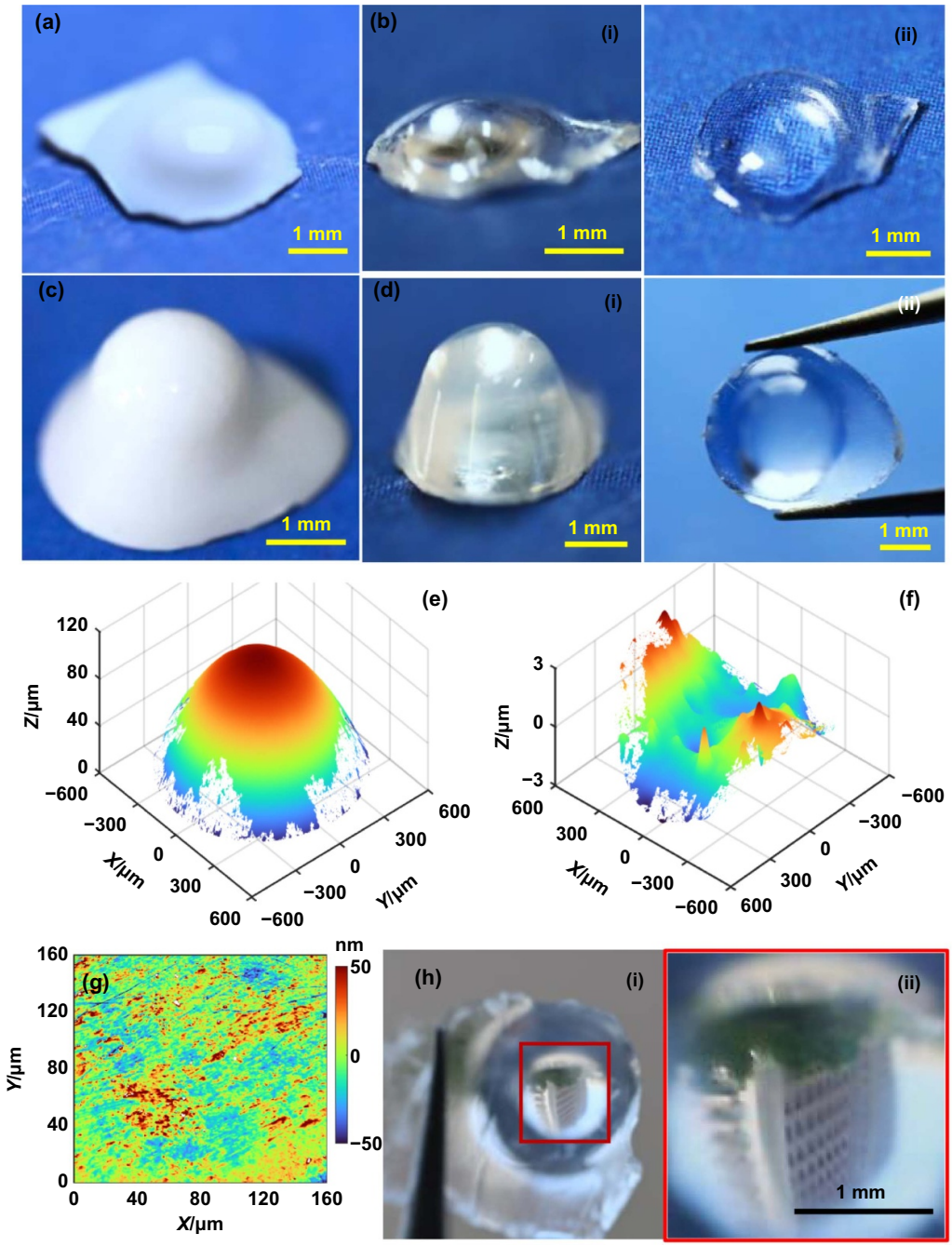

Figure 7. Results for printing spherical fused silica lenses with various curvatures. (a) Printed silica lens after debinding. (b) The sintered clear silica lens as viewed from (i) the side and (ii) the front. (c) The printed silica lens after debinding with a smaller curvature. (d) The sintered clear silica lens with a smaller curvature as viewed from (i) the side and (ii) the front. (e) The 3D form of the clear fused silica lens in (a). (f) The form error after removing the designed shape. (g) The extracted surface roughness component after removing the substrate. (h) The printed lens image: (i) photograph of a building captured through the printed lens, and (ii) its close-up view of the imaged building.

irradiation energy doses was investigated. Minimization and iteration algorithms with nonlinearity compensation were developed to derive the required energy doses for printing. Monte Carlo simulations demonstrated that the time-dependent DLW-based volumetric printing was insensitive to process errors, suggesting that highly precise lenses can be printed with less precise process control.

To showcase the effectiveness of the printing system, a millimeter-scale polymer spherical lens was printed in 5.67 min, achieving a sub-micron form error of about 0.135 μm (RMS) and a sub-nanometric surface roughness of about 0.31 nm (RMS). Additionally, more complex polymer lenses, including lens arrays and freeform lenses, as well as fused silica spherical lenses, were printed, demonstrating the superior capability of the DLW technique for fabricating various lenses with high dimensional accuracy, high surface smoothness, and high printing efficiency.

5. Experimental section

5.1. Experiment setup for the DLW

The self-developed direct laser volumetric printing system primarily consists of a laser module, two-axis motorized precision stages for implementing the planar scanning, and a real-time control system. The practical experimental setup can be found in Video S1, Supplementary Information. The laser modulus (405 nm wavelength and 500 mW power, OXLasers Corporation, China) has a transistor-transistor logic (TTL) interface for receiving the PWM control signals for modulating its output energy doses, and the FWHM of the laser spot was around 0.7 mm. To realize precise raster scanning motions for all the printing, two-step motors (PKP545N18B2, Orientalmotor, Japan) with the motions transmitted by the ball screw slides were controlled in the open-loop mode by tuning the PWM signals. The positioning error along each direction was less than 1 μm, and the scanning speed was set as 0.5 mm·s^{-1} for the printing. The intervals for the dwell points were set as $\delta_x = \delta_y = 20$ μm in the printing.

To coordinate the controlled laser irradiation and the laser raster scanning, the desk-top real-time modulus configured in the Matlab/Simulink was implemented through a high-performance data acquisition board (PCI-6259, NI Corporation, USA). The sampling frequency for the real-time control was set as 20 kHz for the printing. In addition, the periodicity for the PWM signals for the laser and motorized stages in the printing was set as 0.025 s and 0.01 s, respectively. For generating the polymer and fused silica lenses with various shapes, the printing parameters were kept consistent across all cases. Since the laser power is low and the pulse cycle is short, the thermal effects caused by printing in a small region of a few millimeters can be neglected. However, when printing larger lenses with high-power lasers, these thermal effects must be carefully considered to ensure printing accuracy.

Typically, using higher-powered lasers for surfaces with specified shapes allows for faster scanning motions, which may necessitate shorter tuning times for laser irradiation. This can pose challenges for the real-time control system. In the future, a systematic optimization of the printing parameters will be undertaken to achieve an optimal balance between printing efficiency and surface quality.

5.2. Materials

To print polymer lenses, a kind of commercially available clear photocurable resin (Qiefeng Corporation, China) was employed, which had the density and viscosity of around 1.05 g·cm^{-3} and 0.38 Pa·s, respectively. The refractive index of the resin after polymerization was about $n = 1.5$. To print the fused silica lens, the silica nanocomposite was prepared to have the photocurable resin matrix and the silica nanopowders with average diameters of around 40 nm (Aerosi OX50, Evonik Corporation, Germany). The basic resin matrix involved the photoinitiator diphenyl (2,4,6-trimethylbenzoyl) phosphine oxide (TPO), the monomer 2-Hydroxyethyl methacrylate (HEMA), and the coupler triethylene glycol diacrylate (TEGDA). In addition, the 2-Phenoxyethanol (POE) was employed as the solvents to mix those organic materials homogeneously. Considering the debinding and sintering performance of the polymerized silica components, the nanocomposite was optimized to contain 42.69 vol% HEMA, 14.95 vol% POE, 4.23 vol% TEGDA, 0.65 vol% TPO, and 37.5 vol% silica nanopowders. The corresponding theoretical linear shrinkage ratio was estimated to be of 27.67%. For the chemical solvents, the HEMA, POE, and TEGDA were purchased from Meryer Corporation, China, and the TPO was purchased from Yinchang Corporation, China. To achieve homogeneous dispersion for the nanopowders, the solution was firstly stirred for an hour, and the nanopowders were then added dose by dose, during which continuous stirred was implemented with a rotation speed of 800 rpm.

5.3. High-temperature debinding and sintering

For the printing of fused silica lenses, the debinding process was implemented in a high-temperature furnace (KJ-M120-M, Kejia Corporation, China) under atmospheric condition. By referring to the high-temperature processing for the replicated nanocomposites in[41], the green part was held at 150 °C and 300 °C for 4 h each to evaporate water and organics in the printed green bodies. Furthermore, the temperature was increased to 600 °C with heating rate of 2 °C·min^{-1}, which was then held at 600 °C for 120 min to entirely evaporate the organics. After the debinding, the porous brown bodies were further sintered with a low pressure of 0.05 Pa in a vacuum tube furnace (KJ-T1600-L6010LB1, Kejia Corporation, China). The heating rates were selected as 5 °C·min^{-1} from the room temperature to 500 °C, and 3 °C·min^{-1} from 500 °C to 800 °C. The process was held for 90 min at 800 °C. After that, a heating rate of 2 °C·min^{-1} was further employed to slowly heat up to 1 260 °C, dwelling for 2 h to get fully dense and transparent fused silica glasses. The detailed heating profiles for the debinding and sintering are illustrated in Figures 6(b) and (c), respectively.

5.4. Surface and optical property characterization

A CCD camera (SN-60U2K, SangNond Corporation, China) was used for the optical performance characterization, as well as for roughly extracting 2D profiles of the printed structures from the captured 2D images. The CCD camera had 1 392 × 1 024 pixels with each pixel sizing 6.45 μm × 6.45 μm. To capture the 3D form of the printed lenses, a white light interferometer-based optical surface profiler (Newview 8200, Zygo Corporation, USA) was employed, using 20× and 50× objective lenses for characterizing surface forms and surface roughness, respectively. the corresponding lateral resolutions for the measurements were about 0.407 μm and 0.163 μm, respectively. Constrained by the limited field-of-view, the large-area surface forms were stitched by capturing a set of sub-aperture surfaces. During stitching, the overlap ratio was set around 20%, and the captured surface points were automatically registered and fused through the surface processing software *Mx* from Zygo Corporation.

5.5. Algorithm for deriving the duty cycles

As for the DLW-based volumetric printing, the laser energy dose determines the polymerized volume of the resin, including the height and HWFM of the Gaussian-like MGF. The key issue for the precise printing of optics is to accurately derive the duty cycle that controls the energy dose at any dwell point. As discussed in Section 2, the strong nonlinearity between the MGFs and the duty cycles can impose great challenges for deriving the duty cycle distributions required to print optics with specified shapes.

Without loss of generality, a unit duty cycle δ_0 was defined to generate a unit MGF $S(x,y,\delta_0)$. Assume a virtual linear photocuring process that the MGFs are linearly related to the duty cycles, the required duty cycles corresponding to printing the surface $Z(x,\ y)$ can be simply derived by solving the following equation using the linear least square algorithm[32]:

$$\hat{\delta}^{(l)} = \arg\min \| S(x,y,\delta_0) * \delta^{(l)}(x,y) - \hat{Z}(x,y) \|,\ \delta^{(l)}(x,y) \geqslant 0 \tag{4}$$

where * denotes the convolution operation. For a given dwell point (x_m, y_n) in the scanning path, the polymerized volume corresponding to the energy dose with the linear derived duty cycle $\delta^{(l)}_{m,n}$ from Equation (4) can be expressed by[39,40]:

$$V^{(l)}_{m,n} = \delta^{(l)}_{m,n} \cdot \iint S(u,\upsilon,\delta_0)\,\mathrm{d}u\mathrm{d}\upsilon. \tag{5}$$

For the practical nonlinear MGF, the polymerized volume corresponding to the duty cycle $\delta_{m,n}$ can be obtained as[40]:

$$V_{m,n} = \int_0^{\delta_{m,n}} \left(\iint S(u,\upsilon,\delta)\,\mathrm{d}u\mathrm{d}\upsilon \right) \mathrm{d}\delta. \tag{6}$$

For the linearly derived volume $V^{(l)}_{m,n}$, it can be regarded as the desired polymerization volume at the corresponding dwell point (x_m, y_n). Therefore, considering the nonlinearity of the practical MGF, the practical duty cycle $\delta_{m,n}$ for achieving such volume can be obtained by numerically solving the following equation:

$$\delta_{m,n} = \arg\min \left\| V^{(l)}_{m,n} - V_{m,n}(\delta_{m,n}) \right\|,\ \delta_{m,n} \geqslant 0. \tag{7}$$

5.6. Iterative learning algorithm for correcting the duty cycles

The printing of a perfect lens without form error can be treated as the problem of finding a proper duty cycle distribution δ_s that satisfies the following relationship:

$$f(\delta_s(x,y)) = Z(x,y,\delta_s) - \hat{Z}(x,y) = 0. \tag{8}$$

Following the Newton-Raphson method, the optimal duty cycle δ_s can be solved by adopting the following iterations[43]:

$$\delta^{(k+1)}_s(x,y) = \delta^{(k)}_s(x,y) - f(\delta_s) \cdot \left. \frac{\partial \delta_s}{\partial f(\delta_s)} \right|_{\delta_s = \delta^{(k)}_s} \tag{9}$$

where k denotes the iteration step.

In practice, the term $\frac{\partial \delta_s}{\partial f(\delta_s)}$ can be approximately derived by[16]:

$$\left. \frac{\partial \delta_s}{\partial f(\delta_s)} \right|_{\delta_s = \delta^{(k)}_s} \approx \frac{\delta^{(k)}_s(x,y) - \delta^{(k-1)}_s(x,y)}{f\left(\delta^{(k)}_s\right) - f\left(\delta^{(k-1)}_s\right)}. \tag{10}$$

Therefore, by substituting Equations (8) and (10) into Equation (9), the duty cycles can be updated as:

$$\delta^{(k+1)}_s(x,y) \approx \delta^{(k)}_s(x,y) + \left(\hat{Z}(x,y) - \hat{Z}\left(x,y,\delta^{(k)}_s\right) \right) \cdot \frac{\delta^{(k)}_s(x,y) - \delta^{(k-1)}_s(x,y)}{Z\left(x,y,\delta^{(k)}_s\right) - Z\left(x,y,\delta^{(k-1)}_s\right)}. \tag{11}$$

Acknowledgment

This work was supported by the Special funding for Jiangsu Province Innovation Support Program (Grant No. BZ2023058), and the National Natural Science Foundation of China (Grant Nos. 52275437 and U2013211). This article was included in Academic Papers of the 27th Annual Meeting of the China Association for Science and Technology.

ORCID iDs

Limin Zhu https://orcid.org/0000-0003-3194-6731
Zhiwei Zhu https://orcid.org/0000-0001-5363-9797

References

[1] Juodkazis S. 2016. 3D printed micro-optics. *Nat. Photon.* **10**, 499–501.
[2] Camposeo A, Persano L, Farsari M and Pisignano D. 2019. Additive manufacturing: applications and directions in photonics and optoelectronics. *Adv. Opt. Mater.* **7**, 1800419.
[3] Zolfaghari A, Chen T T and Yi A Y. 2019. Additive manufacturing of precision optics at micro and nanoscale. *Int. J. Extrem. Manuf.* **1**, 012005.
[4] Chen X F, Liu W Z, Dong B Q, Lee J, Ware H O T, Zhang H F and Sun C. 2018. High-speed 3D printing of millimeter-size customized aspheric imaging lenses with sub 7 nm surface roughness. *Adv. Mater.* **30**, 1705683.
[5] Hai R H, Shao G B, Ware H O T, Jones E H and Sun C. 2023. 3D printing a low-cost miniature accommodating optical microscope. *Adv. Mater.* **35**, 2208365.
[6] Kotz F, Arnold K, Bauer W, Schild D, Keller N, Sachsenheimer K, Nargang T M, Richter C, Helmer D and Rapp B E. 2017. Three-dimensional printing of transparent fused silica glass. *Nature* **544**, 337–339.
[7] Bauer J, Crook C and Baldacchini T. 2023. A sinterless, low-temperature route to 3D print nanoscale optical-grade glass. *Science* **380**, 960–966.
[8] Cooperstein I, Indukuri S R K C, Bouketov A, Levy U and Magdassi S. 2020. 3D printing of micrometer-sized transparent ceramics with on-demand optical-gain properties. *Adv. Mater.* **32**, 2001675.
[9] Ma X J, Li X Y, Li J Q, Genevois C, Ma B Q, Etienne A, Wan C L, Véron E, Peng Z J and Allix M. 2018. Pressureless

glass crystallization of transparent yttrium aluminum garnet-based nanoceramics. *Nat. Commun.* **9**, 1175.
[10] Xu H, Chen S, Hu R Z, Hu M Q, Xu Y, Yoon Y and Chen Y. 2023. Continuous vat photopolymerization for optical lens fabrication. *Small* **19**, 2300517.
[11] Wang H et al. 2023. Two-photon polymerization lithography for optics and photonics: fundamentals, materials, technologies, and applications. *Adv. Funct. Mater.* **33**, 2214211.
[12] Wen X W et al. 2021. 3D-printed silica with nanoscale resolution. *Nat. Mater.* **20**, 1506–1511.
[13] Wang H et al. 2024. Two-photon polymerization lithography for imaging optics. *Int. J. Extrem. Manuf.* **6**, 042002.
[14] Li Z Y et al. 2024. One-photon three-dimensional printed fused silica glass with sub-micron features. *Nat. Commun.* **15**, 2689.
[15] Ge Q et al. 2021. 3D printing of highly stretchable hydrogel with diverse UV curable polymers. *Sci. Adv.* **7**, eaba4261.
[16] Xu Y, Huang P, To S, Zhu L M and Zhu Z W. 2022. Low-cost volumetric 3D printing of high-precision miniature lenses in seconds. *Adv. Opt. Mater.* **10**, 2200488.
[17] Ge Q, Li Z Q, Wang Z L, Kowsari K, Zhang W, He X N, Zhou J L and Fang N X. 2020. Projection micro stereolithography based 3D printing and its applications. *Int. J. Extrem. Manuf.* **2**, 022004.
[18] Wu L and Dong Z C. 2023. Interfacial regulation for 3D printing based on slice-based photopolymerization. *Adv. Mater.* **35**, 2300903.
[19] Wu J J, Guo J, Linghu C H, Lu Y H, Song J Z, Xie T and Zhao Q. 2021. Rapid digital light 3D printing enabled by a soft and deformable hydrogel separation interface. *Nat. Commun.* **12**, 6070.
[20] Shan Y J, Hua J Y and Mao H C. 2024. 3D printing of optical lenses assisted by precision spin coating. *Adv. Funct. Mater.* **34**, 2407165.
[21] Zhang Y, Wu L, Zou M M, Zhang L D and Song Y L. 2022. Suppressing the step effect of 3D printing for constructing contact lenses. *Adv. Mater.* **34**, 2107249.
[22] Kelly B E, Bhattacharya I, Heidari H, Shusteff M, Spadaccini C M and Taylor H K. 2019. Volumetric additive manufacturing via tomographic reconstruction. *Science* **363**, 1075–1079.
[23] Toombs J T, Luitz M, Cook C C, Jenne S, Li C C, Rapp B E, Kotz-Helmer F and Taylor H K. 2022. Volumetric additive manufacturing of silica glass with microscale computed axial lithography. *Science* **376**, 308–312.
[24] Webber D, Zhang Y J, Sampson K L, Picard M, Lacelle T, Paquet C, Boisvert J and Orth A. 2024. Micro-optics fabrication using blurred tomography. *Optica* **11**, 665–672.
[25] Shusteff M, Browar A E M, Kelly B E, Henriksson J, Weisgraber T H, Panas R M, Fang N X and Spadaccini C M. 2017. One-step volumetric additive manufacturing of complex polymer structures. *Sci. Adv.* **3**, eaao5496.
[26] Orth A et al. 2023. Deconvolution volumetric additive manufacturing. *Nat. Commun.* **14**, 4412.
[27] Darkes-Burkey C and Shepherd R F. 2024. Volumetric 3D printing of endoskeletal soft robots. *Adv. Mater.* **36**, 2402217.
[28] Regehly M, Garmshausen Y, Reuter M, König N F, Israel E, Kelly D P, Chou C Y, Koch K, Asfari B and Hecht S. 2020. Xolography for linear volumetric 3D printing. *Nature* **588**, 620–624.
[29] Hahn V, Rietz P, Hermann F, Müller P, Barner-Kowollik C, Schlöder T, Wenzel W, Blasco E and Wegener M. 2022. Light-sheet 3D microprinting via two-colour two-step absorption. *Nat. Photon.* **16**, 784–791.
[30] Stüwe L, Geiger M, Röllgen F, Heinze T, Reuter M, Wessling M, Hecht S and Linkhorst J. 2023. Continuous volumetric 3D printing: xolography in flow. *Adv. Mater.* **36**, 2306716.
[31] Loterie D, Delrot P and Moser C. 2020. High-resolution tomographic volumetric additive manufacturing. *Nat. Commun.* **11**, 852.
[32] Axinte D and Billingham J. 2019. Time-dependent manufacturing processes lead to a new class of inverse problems. *Proc. Natl Acad. Sci. USA* **116**, 5341–5343.
[33] Axinte D, Billingham J and Guillerna A B. 2017. New models for energy beam machining enable accurate generation of free forms. *Sci. Adv.* **3**, e1701201.
[34] Zuo J X and Lin X C. 2022. High-power laser systems. *Laser Photon. Rev.* **16**, 2100741.
[35] Cakmakci O, Moore B, Foroosh H and Rolland J P. 2008. Optimal local shape description for rotationally non-symmetric optical surface design and analysis. *Opt. Express* **16**, 1583–1589.
[36] Tang H S, Li H R, Feng Z X, Luo Y and Mao X L. 2024. Differentiable design of a double-freeform lens with multi-level radial basis functions for extended source irradiance tailoring. *Optica* **11**, 653–664.
[37] Wang T Y et al. 2021. Universal dwell time optimization for deterministic optics fabrication. *Opt. Express* **29**, 38737–38757.
[38] Kim D W, Kim S W and Burge J H. 2009. Non-sequential optimization technique for a computer controlled optical surfacing process using multiple tool influence functions. *Opt. Express* **17**, 21850–21866.
[39] Su X and Yue X B. 2022. Nonlinear dwell-time algorithm for freeform surface generation by atmospheric-pressure plasma processing. *Opt. Express* **30**, 18348–18363.
[40] Su X, Ji P, Jin Y, Li D, Qiao Z, Ding F, Yue X B and Wang B. 2021. Freeform surface generation by atmospheric pressure plasma processing using a time-variant influence function. *Opt. Express* **29**, 11479–11493.
[41] Du X T, Xu Y, Liu H, Li Z L, Zhu L M and Zhu Z W. 2023. Precise and rapid replication of complex-shaped fused silica optics. *Adv. Opt. Mater.* **11**, 2300840.
[42] Kotz F et al. 2016. Liquid glass: a facile soft replication method for structuring glass. *Adv. Mater.* **28**, 4646–4650.
[43] Ypma T J. 1995. Historical development of the newton–raphson method. *SIAM Rev.* **37**, 531–551.